Title
Effect of cell compression on the performance and the structure of proton exchange membrane water electrolyzer (PEMWE) assembly

Journal
Electrochimica Acta, 547

ISSN
0013-4686

Authors
Tolouei, Nadia E
Chabot, Florian M
Yang, Patrick
et al.

Publication Date
2026

DOI
10.1016/j.electacta.2025.147871

Effect of cell compression on the performance and the structure of proton exchange membrane water electrolyzer (PEMWE) assembly

Nadia E. Tolouei[1,*], Florian M. Chabot[1,2,*], Patrick Yang[1], Jack T. Lang[1], Bjorn Hasa[3], Utsav Raj Aryal[3], Gaohua Zhu[3], Dilworth Y. Parkinson[2] and Iryna V. Zenyuk[1,+]

1. Department of Chemical and Biomolecular Engineering, National Fuel Cell Research Center, University of California Irvine, Irvine, CA 92697
2. Advanced Light Source, Lawrence Berkeley National Laboratory, Berkeley, California, 94720
3. Toyota Research Institute of North America, Ann Arbor, Michigan 48105

*Contributed equally

+Corresponding author: Iryna.zenyuk@uci.edu

Abstract:

In the field of water electrolysis, the proton exchange membrane water electrolyzer (PEMWE) is currently the most advanced technique for producing hydrogen without emitting CO_2. Although PEMWE plants are already in operation, further research is needed to improve cell efficiency and reduce the use of rare materials, such as iridium oxide catalysts for the oxygen evolution reaction (OER). One of the main causes of performance loss in PEMWE is the relatively low conductivity of the porous transport layer (PTL) and of the anode catalyst layer, which results in ohmic losses and low catalyst utilization during high current density operation. The objective of this study is to investigate how optimization of the PTL and electrode interface can increase the cell performance. To this end, we tested different cell assemblies using fibrous and sintered PTLs, decreasing

membrane thickness, reducing iridium loading, and inserting a microporous layer to increase contact surface area. Electrochemical characterization of each cell configuration was systematically performed at various compression levels as the pressure is a crucial parameter influencing the electrode/PTL contact area. In parallel, microcomputed tomography (micro-CT) was employed to investigate the effects of cell hydration and compression on the structure of PEMWE components. This study combining electrochemistry and micro-CT imaging presents how optimizing the electrode/PTL contact surface area, minimizes ohmic losses, and enables PEMWE operation with low iridium loading at high current densities.

Introduction:

Hydrogen is essential for industrial processes like ammonia synthesis, methanol production, and oil refining, but most of it is still produced via methane reforming, leading to high CO_2 emissions[1,2]. In addition, hydrogen is seen as a clean energy carrier to support decarbonization, enhance renewable energy storage, and develop a green alternative for long-range transportation[3]. To reach net-zero emissions by 2050, the actual hydrogen production is expected to be multiplied by 4, resulting in 530 million metric tons of global production, potentially cutting 7 gigatons of CO_2 emissions annually[4]. Water electrolysis coupled with renewable power generation is the best solution to decarbonize hydrogen production. Among the several existing technologies, the proton exchange membrane water electrolyzer (PEMWE) is highly compatible with fluctuating and intermittent energy sources, enabling efficient hydrogen production at high current densities with exceptional gas purity making it a promising technology for research, industry adoption, and large-scale commercialization[4,5]. The state-of-the-art PEMWE assembly is composed of two

conductive porous layers, depicted Figure 1,the titanium-based porous transport layer (PTL), allowing water and oxygen to diffuse, and the gas diffusion layer (GDL), facilitating hydrogen removal. The PTL and GDL are, respectively, in contact with, the iridium oxide-based anode catalyst layer, and the cathode electrode made from carbon supported platinum nanoparticles. These two electrodes are separated by a proton-conducting membrane. Even though PEMWE is a mature technology improvement of their efficiency is required to bring down the hydrogen cost.

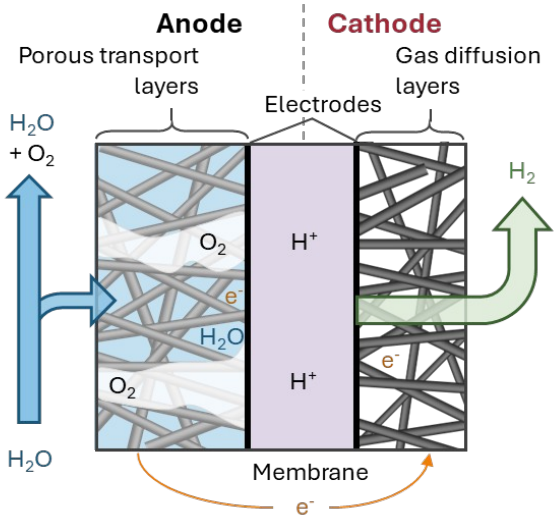

Figure 1. Schematic of the state-of-the-art PEMWE main components and the resulting transport of species.

In PEMWE, different overpotentials or voltage losses contribute to the final cell potential. Among the various overpotential losses, ohmic resistance is one of the most significant factors reducing the overall cell performance[6,7]. Ohmic losses result from electron conductivity and proton transport. Electronic resistivity primarily comes from the anode catalyst layer, where the iridium oxide (IrO_2) based catalyst layer has relatively poor electronic conductivity[8], and from the titanium PTL [9], that passivates under PEMWE operating condition. Despite the relatively low intrinsic conductivity of the material, minimizing ohmic losses can be achieved by improving the interface between the

electrode and the PTL or by reducing the membrane thickness. However, using thin membranes introduces challenges such as increased hydrogen permeation and loss of Faradaic efficiency.

Garcia-Salaberri et al.[10] highlight the key role of the PTL/electrode interfacial contact in the distribution of metallic potential across the membrane electrode assembly (MEA) surface and in the resulting catalyst utilization. Due to the low conductivity of iridium oxide electrodes, their in-plane electron transport can become limiting, especially at high current density and for electrodes with low loading of iridium [11]. One solution to improve interfacial contact is by changing the PTL structure or by inserting microporous layer (MPL) to maximize the contact surface area with the electrode[12]. Another way to improve interfacial contact and reduce ohmic loss is by increasing the cell assembly compression[7]. From the literature, several studies showed that the optimal cell compression is reached for an average pressure of 1.5 to 3 MPa [9,12,13], while the pressure is heterogeneously distributed due to the flow field pattern and the PTL surface morphology [14,15,16]. However, it has been shown that modifying the flow-field pattern and using an additional thicker PTL significantly helps distribute pressure more evenly across the surface area of the catalyst layer [14].

While increasing the pressure improves the interfacial contact resistance[17,18], excessive compression leads to higher hydrogen crossover[10,11] due to reduced membrane thickness and loss of the electrolyzer efficiency. The same tradeoff between performance and hydrogen permeation has been shown on stack assembly by Siracusano *et al.* [19] when investigating the optimal components and assembly characteristics for PEMWE. Analyzing the mechanical behavior of individual cell components, Arthurs and Kusoglu [20] show that in the typical range of pressure applied in PEMWE both the GDL and the membrane are deforming. Olesen and Kær [21] developed a model

assessing the impact of membrane compression on water uptake and PEMWE performance, revealing that increased compression reduces water uptake and raises cell voltage. Focusing on the membrane, Hintzen *et al.* studied the effect of compression, focusing on more even pressure distribution across the active surface area and comparing the effect of wet versus dry assembly [14]. Increasing the pressure, having uneven pressure distribution and assembling the MEA under dry conditions are all factors causing durable deformation of the membrane and its creeping. Cruz Ortiz *et al.* [15] observed that, throughout the membrane, land regions exhibit a broader thickness deviation than channel regions due to membrane deformation caused by intrusion into the PTL. This effect becomes more pronounced with increasing compression. In addition, Holzapfel *et al.[16]* demonstrated that thin membranes deform more than thicker membrane with compression. Bazarah *et al.[17]* explored key parameters affecting PEMWE performance, emphasizing that while increased compression reduces electric contact resistances, excessive pressure combined with rising temperatures can lead to hot spots and accelerated degradation. Cruz Ortiz et al. [15] further investigated the effect of compression on membrane durability and found that compression range of 30-40%, relatively to the GDL, yields optimal results, whereas compression exceeding 60% leads to accelerated membrane degradation[14,15]. Therefore, it is crucial to optimize the compression level to achieve a balance between interfacial contact and controlled hydrogen permeation for PEMWE.

Optimization of the PEMWE compression is mandatory to increase the stack efficiency. Too few materials and pressure ranges were investigated to have a broad understanding of the role of compression on the electrolyzer operation. Even though the mechanical behavior of each individual material has been studied, studies on the mechanical deformation of the cell are missing. Thus, this study investigates the effect of compression on structure and performance of PEMWE for a broad

range of pressure and for various materials. Through electrochemical characterization, this study depicts the effect of cell compression on the performance and high frequency resistance (HFR). Different cell configurations were used, comparing sintered titanium PTL with fiber titanium PTL and using both Nafion 115 and Nafion 212 to investigate the interplay between membrane thickness and compression. In parallel, micro computed tomography (micro-CT) was used to image the cell assembly across a broad range of pressure to access the deformation of the components. Finally, electrochemical characterization was performed on the anode catalyst layer having a low (0.39 mg_{Ir}/cm^2) and an ultra-low loading (0.14 mg_{Ir}/cm^2), while introducing a micro porous layer to increase the interfacial contact area.

Methods:

MEA preparation

The catalyst ink was prepared using Nafion D2021 as a binder and rutile IrO_2 (TEC77110, Tanaka) catalyst powder. Catalyst was introduced in the solvent mixture made with n-propanol and DI-water with a weight ratio of 0.5. Ionomer dispersion was then added to reach a catalyst weight ratio of 0.15. The total weight content of the ink was set at 0.25. The electrode layers were deposit onto a polymer substrate (PTFE) using the blade coating method at a speed of 20 mm/s with a 110 µm bar gap. Cathode electrode was provided by an industrial partner with a loading of 0.367 mg/cm^2 and Pt/C weight ratio of 0.5. MEAs were assembled by hot-pressing the electrode decals onto the Nafion membrane following a two-step process, where temperature is equilibrated at 134°C for 5 minutes without applied pressure followed by a pressure hold at 4 MPa for 10 minutes. The loading of the

electrodes was determined by weighing the decal before and after the electrodes transfer. Each cell was assembled with a Freudenberg H23C6 GDL on the cathode side and a titanium PTL on the anode side. Several configurations of cell were used to investigate the role of the PTL structure, the membrane thickness and the anode loading. The PEMWE configurations, and their denominations are summarized in Table 1. Two types of PTLs were used, a sintered titanium PTL from Mott of 263 µm thickness with an average pore radius of 6.2 µm, and a titanium fiber PTL of 274 µm thickness, provided by an industrial collaborator. Effect of compression on performance was first investigated on MEA with iridium loading of 0.39 mg/cm^2. The comparison between two types of PTLs was made with the samples "Sintered PTL N212" and "Fiber PTL N212". A thicker membrane was used for the "Sintered PTL N115" for comparison. In addition, for the lower iridium loading of 0.14 mg/cm^2, the "Sintered PTL N212" MEA was compared to the "Sintered MPL N212" configuration having a microporous layer (MPL) from DeNora, with an average pore radius of 1.9 µm, at the interface between the Sintered PTL and the catalyst layer.

***Table 1**. Summary of the samples, their denominations, and their main characteristics.*

Sample	PTL	Membrane	Loading *[mg/cm²]*
Sintered PTL N212	Sintered	N212	0.39
Fiber PTL N212	Fiber	N212	0.39
Sintered PTL N115	Sintered	N115	0.39
Sintered PTL N212	Sintered	N212	0.14
Sintered MPL N212	Sintered + MPL	N212	0.14

Cell assembly

The MEA was tested with a Scribner cell having a triple serpentine flow field with a channel and land width of 1 mm and 0.85 mm, respectively. The active surface area was delimited to 5 cm^2 by a Kapton subgasket of 25 μm thickness. PTL and GDL were cut 1 mm larger than the delimited active area on each dimension for edge-protection. The schematic of the cell assembly is shown in **Figure S1** of Supporting Information (SI). Gaskets were cut from Kapton and PTFE to the cell geometry, with an opening at the center to align the PTL and the GDL with the active surface area. At the cathode side, the gasket thickness was set at 20% of the GDL thickness. The compression of the assembly was controlled by the thickness of the gasket at the anode side. The same MEA was tested for each compression step. Instead of fully disassembling the cell, all layers were kept in place as much as possible without being completely separated. Only the gasket layer was removed and replaced with one of a different thickness. Care was taken to maintain the alignment and position of the other components to ensure consistency. The cell was initially assembled with a gasket thickness

matching the PTL thickness. After the electrochemical characterization, the gasket thickness was adjusted based on the intended compression factor as defined in Equation 1:

$$Compression\ factor = \left(\frac{T_{PTL} - T_{gasket}}{T_{PTL}} \right) \times 100 \quad (1)$$

with T being the thickness. The cell was reassembled and tested again at higher compression. The torque applied to each of the cell's 8 bolts was kept at 7.9 N.m. Considering the force is distributed at the surface of the PTL and GDL (7.29 cm^2) only, the maximum pressure applied is estimated to be about 19.5 MPa with this torque.

Electrochemical characterization

The electrochemical protocol was performed with a Kolibrik (PTC-05100EW) power supply. Electrochemical characterization included polarization curves, electrochemical impedance spectroscopy (EIS) and cyclic voltammetry (CV). Characterization was carried out at a cell temperature of 60°C and under atmospheric pressure, with a water flow rate of 2 $mL \cdot min^{-1} \cdot cm^{-2}$ at the anode. Cathode was flushed with 10 mL/min of hydrogen to maintain the potential of the reference hydrogen electrode. Each fresh MEA were conditioned only at the first compression step by cycling 500 times the voltage between 0.01 V and 1.3 V at a scan rate of 2 V/s and then by holding the current density at 2 A/cm^2 for 2 hours.

Electrochemical protocol was then applied at each compression step. 10 cycles of CVs were performed at scan rates of 25, 50, 75, and 100 mV/s from 0.01 to 1.3 V vs. RHE (**Figure S2**). The

CVs at 50 mV/s were used to measure the charge density of the catalyst layer. CV were integrated through the whole voltage range. The resulting charge was divided by two and by the iridium loading to get a specific charge density, per catalyst weight, to compare the charge of electrode having different loading. To capture the effect of compression, the charge was divided by the initial charge measured at 0 % compression factor (**Figure S3**). Polarization curves were measured with chronoamperometry, from 1.3 to 2.2 V, holding the voltage for 1 min to extract the corresponding stabilized current. The polarization curves of two independently prepared cells demonstrated good reproducibility (**Figure S4**). Minor deviations in the raw data were due to ohmic losses, as the overlapping HFR-corrected curves indicated reproducibility. This suggested that differences mainly arose from interfacial contact resistance, confirming reproducible electrode preparation. At each voltage step, EIS were measured from 20 kHz to 1 Hz to determine the high frequency resistance (HFR) from the real impedance value corresponding to the null imaginary impedance as presented as an example in **Figure S5** for the Sintered PTL N212 sample. The accuracy of the HFR measurement depends heavily on the quality of the EIS spectra and the extraction method used. The quality of the EIS spectra was verified across the compression range (Figure S5a), and the HFR was consistently estimated by interpolation throughout the experiments (Figure S5b). Therefore, it is assumed that the HFR measurement is minimal and lies below 1 $m\Omega \cdot cm^{-2}$, which corresponds to the maximum difference in real impedance between the two impedance measurements used for HFR interpolation. Furthermore, the discussion of the results will focus primarily on the effect of compression on the HFR extracted using the same measurement protocol applied to the same MEA. This prevents measurement error from affecting the results discussed. For better readability, the average HFR will also be reported for each compression factor by measuring the mean HFR across

the current density range. At each voltage step (U), the HFR was used to correct the polarization curves for ohmic losses ($U_{corr.}$) according to Equation 2:

$$U_{corr} = U - j \times HFR \quad (2)$$

with the current density j and the HFR normalized by the active surface area. Due to time and material limitations, the reproducibility error of the sample performance could not be assessed for all sample configurations. Therefore, the deviation in performance and HFR from sample-to-sample comparisons will be treated carefully for minor variations.

Pressure paper used to measure heterogeneity of pressure distribution

The contact pressure distribution over the active area of the test cell was evaluated using pressure measurement film from Fujifilm® having a pressure range sensitivity from 2.4 to 9.5 MPa. To replicate the compression applied to the cell components, the cell was assembled repeatedly with the same Sintered PTL N212 configuration and a consistent torque of 7.9 Nm. During each assembly, a pressure sensitive film was positioned at the interface between the PTL and the flow field. To achieve the intended compression factor, the gasket thickness was systematically adjusted for each test. The pressure sensitive films analysis enabled a clear representation of the pressure distribution across the active surface area. Images of the pressure sensitive film after compression are presented in **Figure S6** of the SI. Image analysis was carried out with ImageJ. Images were converted into grey scale values to determine the pressure from pixel intensity. An uncompressed region and an over compressed region were used to determine the pixel values corresponding to the pressure limits of the films, respectively, 2.4 and 9.5 MPa. Images were then converted into the pressure maps displayed in **Figure S7** using the pixel intensity distribution and the higher and lower values

213 determined as boundary values corresponding to the highest and lowest pressure limits of the
214 pressure sensitive film.

215 **X-ray Computed Tomography Setup**

216 X-ray micro computed tomography (micro-CT) was conducted at the Beamline 8.3.2 of the
217 Advanced Light Source (ALS). The beamline was operated in white light mode with a x-ray
218 spectrum having a median energy of 30 keV. The images were acquired using a 20 μm LuAg
219 scintillator, a 10X magnification lens, and a sCMOS PCO Edge camera resulting in images with a
220 pixel size of 0.635 μm/pixel. Tomographs were reconstructed from 1313 projections acquired with
221 an exposure time of 80 ms. The resolution of reconstructed tomographs is about 3 to 6 μm,
222 depending on the scan and the location within the image stack. Two tomography cells were designed
223 specifically to image the deformation of the electrolyzer components with compression. Both cells
224 have a single linear channel that varies in width, from 0.65 mm for one cell to 1 mm for the other cell.
225 In the following sections, the cells will be referred to as "0.65 mm Cell" and "1 mm Cell". The
226 membranes were cut to the cell dimension. PTL and GDL having dimensions of 1.7x15 mm^2 were
227 aligned using Kapton gaskets. Gasket thickness of 170 μm and 127 μm were used at the anode and
228 cathode side, respectively, to allow the deformation of the component's assembly upon stress. A
229 schematic of the cell assembly for micro-CT study is shown in **Figure S9**. The effect of deformation
230 was studied over two membrane thicknesses (Nafion N115 and Nafion NR212), two types of PTLs
231 (Mott Sintered PTL and Fiber PTL) and two channel width (1 mm and 0.65 mm). In total 8 cell
232 configurations were imaged at several pressures. Each cell was initially assembled dry, with bolts
233 being hand tight, imaged and then flushed with DI water at temperature about 32 to 38 ^{o}C for at least
234 20 minutes before imagining the wet assembly. Tomographs were then measured at 4 stages of

compression, defined by the torque values of 5 N.cm, 8.5 N.cm, 13 N.cm and 17 N.cm applied on the 4 bolts.

Image analysis

To determine the pressure inside the cell for each condition the thickness of the GDL under the land was measured for each tomograph. A stress-strain curve of the GDL was measured on GDL samples of 5 mm diameter with a compression stage equipped with a load cell. The thickness of the GDL was used in parallel to its stress-strain curve to estimate the GDL stress and thus the overall stress of the cell assembly under the land. The cell configuration and the pressure applied at each condition, spanning between 4 and 14 MPa, are summarized in **Figure S10**.

Image analysis process was developed and applied to all tomographs to quantitatively study the deformation of the GDL, membrane and PTL. The process is presented in the SI, with the analysis steps depicted in the **Figure S11-a** for the PTL and **Figure S11-b** for the GDL. The process was performed over at least 360 slices of the tomographs to depict the overall structure change throughout the imaged volume. Image filtering was applied to improve the quality and the contrast of the images. At the PTL side, pixel outliers were removed with a median filter. For the GDL side, the contrast of the carbon with the surrounding was enhanced using a gamma correction filter and a non-linear median filter was applied to smooth the objects surfaces while preserving their edges. Then, the texture of the image was improved with a non-local mean filter. Pixel outliers were finally removed using a median filter. This filtering process was necessary to ensure proper thresholding. Different threshold algorithms were applied depending on the tomograph to obtain a final binary

image where porous layers appear in white within black regions corresponding to pores and surroundings. Finally, from each binary image, the pixel position of the first and last PTL or GDL objects were determined across the image length to plot the surfaces of the PTL and GDL on the membrane and on the channel side. The position of the surfaces of the PTL and GDL were averaged across the tomograph to obtain the overall position in the imaged volume, as plotted in **Figure S11**. The resulting curves were fitted with a fourth order polynomial that are used in the following to plot the components deformation across the channel length. As the low contrast between the membrane and the carbon is preventing us from determining accurately the position of the membrane/MPL interface, only the GDL surface facing the channel is used to analyze the cell deformation.

Results:

Electrochemistry

First, we present the resutls of the compression study with thin N212 membrane and two types of PTLs: sintered and fiberous. **Figure 2a** presents the polarization curves of the Sintered PTL MEA when increasing the compression factor from 0% to 40%. The polarization curves, without additional compression, aligned well with values previously reported in the literature for similar IrOx catalyst loadings[22]. A clear improvement in polarization was observed as the compression increased, with optimal cell performance achieved at 28% compression. Polarization curves corrected with the HFR are overlapping, indicating that the performance improvement with compression results directly from the HFR decrease with higher compression. In PEMWE, the HFR accounts for the electronic conductivity of all the components and for the proton transport within the membrane. Here, the electronic resistance results mostly from the anode components because of the low conductivity of the IrO_2 electrode and of the titanium PTL[8]. In comparison, the electric

278 resistance of the components at the cathode side is low. Therefore, the decrease in HFR and the
279 improvement of the performance must result from improved interfacial contact at the PTL/electrode
280 interface and/or membrane thinning, as it flows into the pores of the PTL and into the locations of the
281 cathode channel, as will be discussed more in detail in later sections.

282 The evolution of HFR with compression and current density is presented in Figure 2**b**. At the lowest
283 compression factor (0%), the HFR increases noticeably with current density. As the cell
284 compression factor increases, the overall HFR decreases, while it becomes more stable with current
285 density. The lowest HFR is observed at the optimal compression factor of 28% while increasing
286 further the compression (e.g., to compression factor of 40%) leads to a slight increase in HFR,
287 possibly due to mechanical deformation of the electrode or of the membrane previously observed in
288 the literature[14]. Membrane conductivity is also a function of compression, as at higher
289 compression water channels can collapse resulting in lower in-plane conductivity [30]. The effect of
290 compression on HFR is shown in **Figure 2c** that presents the average HFR calculated as the mean of
291 HFR measured throughout the current density range for each compression factor. Increasing the
292 compression factor to 28% results in a decrease in the average HFR from 76 to 61 $m\Omega \cdot cm^{-2}$. In
293 comparison to the membrane resistivity of fully hydrated Nafion 212 (50 μm thickness), this
294 additional 11 $m\Omega \cdot cm^{-2}$ is most likely due to electron contact resistances.

295 Then, we investigated the effect of different compression factors on cells assembled with a Fiber
296 PTL to assess whether a PTL with a smaller contact surface area influences performance. The
297 polarization curves of Fiber PTL in Figure 2**d**, show a similar trend as observed for Sintered PTL,
298 where increasing compression improved cell performance, with an optimum compression factor of
299 28%. The overlapping of the HFR-corrected curves shows that the change in performance with

compression mostly results from the HFR. The evolution of HFR, averaged across the current density range, with compression is presented in the Figure 2**e.** It shows HFR decreasing with compression. Similarly to the results from the Sintered PTL, the minimum of averaged HFR was observed about 20 to 28% compression factor, as shown in Figure 2**f**, while the evolution in HFR with higher compression remains small. At the optimal compression factor of 28%, the HFR is 61 $m\Omega \cdot cm^2$ for the Sintered PTL and 71 $m\Omega \cdot cm^2$ for the Fiber PTL. This difference of 10 $m\Omega \cdot cm^2$ must results from the better interfacial contact area for Sintered PTL compared to Fiber PTL. Indeed, the image analysis revealed that the porosity of the Fiber PTL of 63% was much higher than the 37% porosity measured for the Sintered PTL. For both PTLs, the average HFR for different compression factors remains above the resistance of the fully hydrated Nafion 212 membrane (50 $m\Omega \cdot cm^2$)[23].

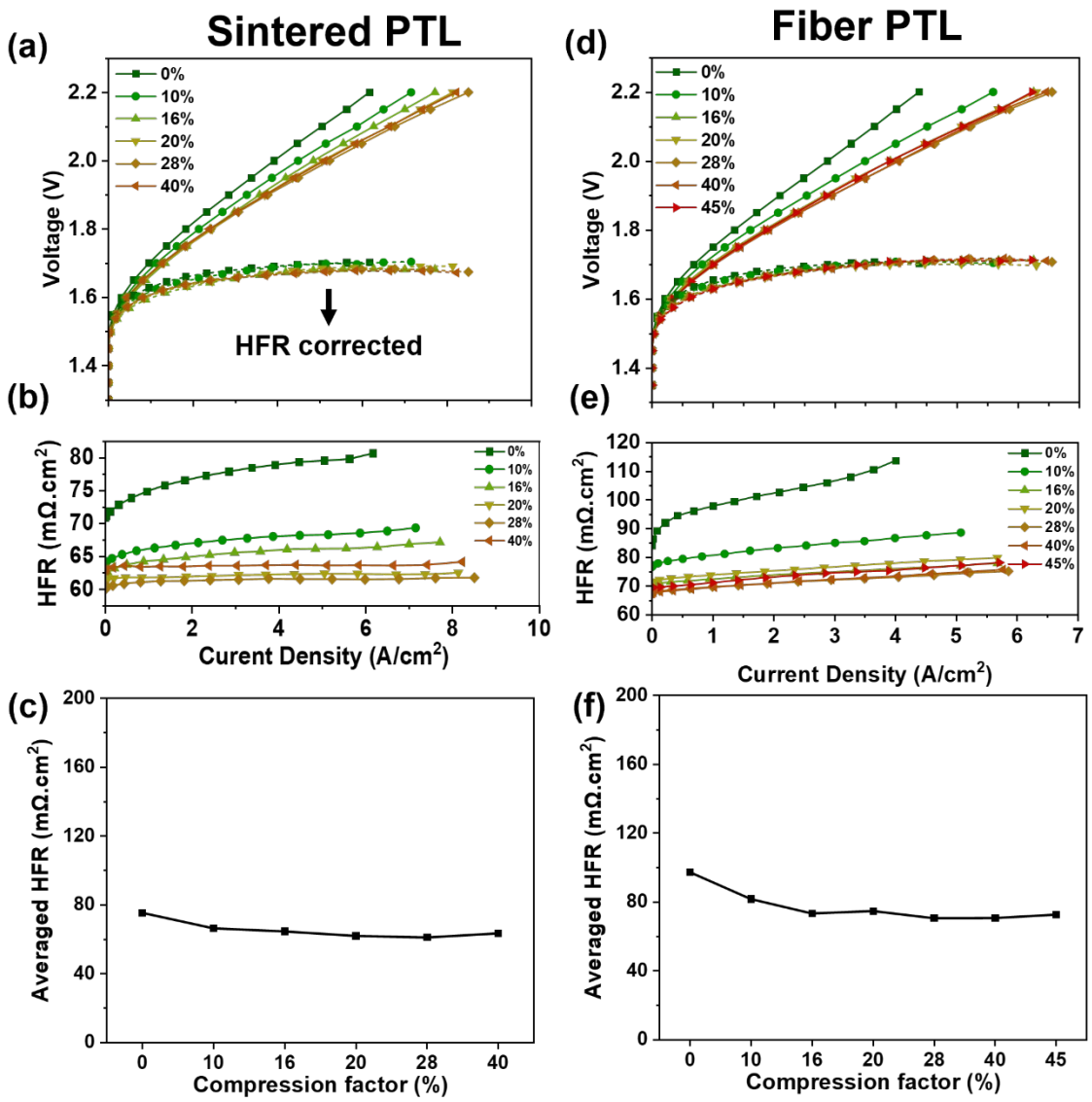

310

311 ***Figure 2.*** *Electrochemical characterization data for low loading (0.39 mg/cm²) Sintered PTL with*

312 *Nafion 212 membrane. a) Polarization curve b) HFR vs current density. c) Averaged HFR as a*

313 *function of compression factor. Fiber PTL with Nafion 212 membrane d) Polarization curve e) HFR*

314 *vs current density. f) Averaged HFR as a function of compression factor.*

315 After establishing the influence of compression on cells assembled with a thin membrane, the study

316 was extended to examine how compression factor affects MEA performance when using a thicker

membrane (Nafion 115, 125 μm thickness). Similar to previous observations, the cell assembled with Sintered PTL and N115 (Figure 3**a**) shows noticeable improvement in polarization when increasing the compression factor up to a similar compression factor, of about 20 to 28%. The improved performance at 28% compression appears to result from a reduction in HFR (Figure 3**b**). However, above 28% the HFR increases significantly, which might be due to catalyst layer porosity change or membrane conductivity decrease [30]. The average HFR measurement confirms this (Figure 3**c**), decreasing by 4 mΩ.cm² from 10% to 28% compression and increasing by 7 mΩ.cm² from 28% to 40%. This improvement in performance is related to the decrease in HFR due to enhanced interfacial contact. Similar resistivity decreases were measured for both the thin (Sintered PTL N212) and thick (Sintered PTL N115) membranes between 10% and 28% compression, at 4 and 6 mΩ.cm², respectively, confirming that the decrease in HFR is not related to improved proton transport. Surprisingly, for Sintered PTL with Nafion 115 membrane, the average HFR through different compression factors remains below the 130 mΩ.cm^2 resistance of the fully hydrated Nafion 115 membrane[24].

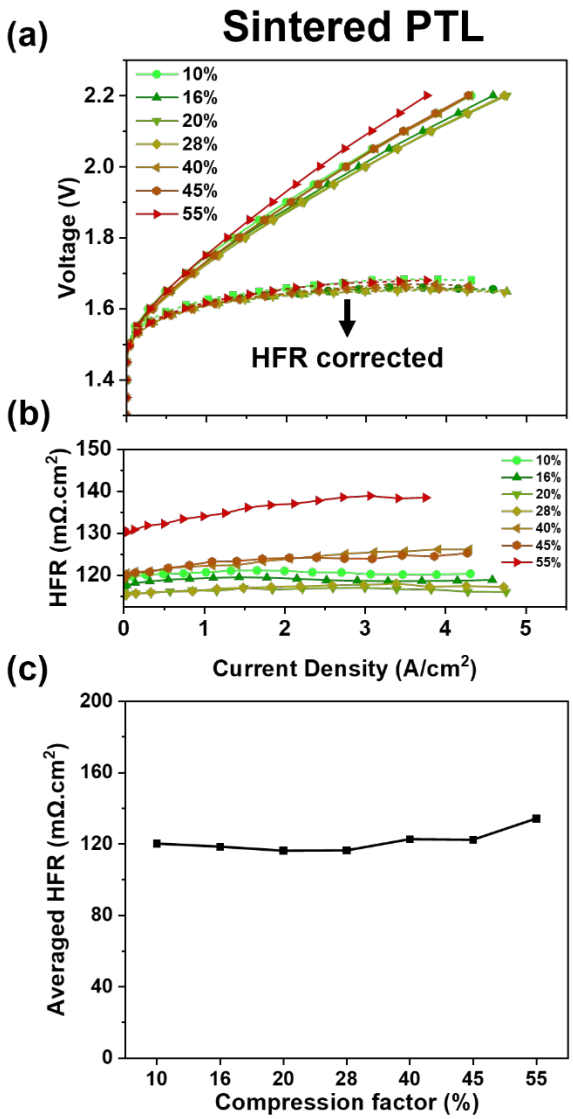

331

332 ***Figure 3***. *Electrochemical characterization data for low loading (0.39 mg/cm^2) Sintered PTL with*
333 *Nafion 115 membrane. a) Polarization curve b) HFR vs current density. c) Averaged HFR as a*
334 *function of compression factor.*

335 The next phase of this study examines the effects of significantly reducing iridium loading from 0.39
336 to 0.14 mg/cm². For the lower loading, the interfacial contact between catalyst layer and porous
337 transport layer becomes critical due to the potential decrease in catalyst particle connectivity and due

to the higher sheet resistance, which is inversely proportional to thickness. Considering the electrode thickness is proportional to iridium loading, the sheet resistance is inversely proportional to iridium loading. For catalyst layers with high sheet resistance MPL addition can better connect IrOx particles, increasing in-plane electric conductivity. Two MEAs were tested with the low iridium loading of 0.14 mg/cm^2, one with a Sintered PTL (Sintered PTL N212 membrane) and then the same configuration with the addition of an MPL (Sintered MPL N212 membrane). Figure 4**a** shows the polarization curves for the Sintered PTL N212 with 0.14 mg/cm^2 anode catalyst layer loading. At the lowest compression of 0%, the cell performance is lower in comparison to the MEA with a higher loading (0.39 mg/cm^2). Polarization curves are improved when increasing the compression factor, with the optimal compression factor found at 28% as observed previously in the other configurations using higher loadings. Additional compression offers no further benefit. Under optimal compression, the MEA performance was very close to what was measured for the higher loading. At 2 V, the cell with 0.14 mg_{Ir}/cm² reaches 3.85 A/cm², while the cell reached 4.5 A/cm^2 with a loading of 0.39 mg/cm² (Figure 3**-a**). The performance improvement with compression results from the decrease in HFR shown in Figure 4**b**. The evolution of averaged HFR, displayed in Figure 4**c,** confirms that optimal performance is achieved when HFR is the lowest, at 28% compression factor. As shown in **Figure 2c**, the HFR for the higher loading (0.39 mg/cm²) decreased modestly from 70 to 61 mΩ·cm² between 0–28% compression, while the lower loading electrode (0.14 mg/cm²) showed a larger HFR decrease from 123 to 71 mΩ·cm². For the low loading electrode, the strong decrease of HFR with compression indicates that contact resistance impact HFR more significantly.

To further increase interfacial contact area, the Sintered PTL was tested with the incorporation of an MPL. Figure 4**d** shows the polarization curve for this configuration up to 16% compression factor

that corresponds to the optimal performance. Compression was not increased further since no significant improvement in performance was seen between compression factors of 10% and 16%. Under optimal compression the cell reaches 4.7 A/cm² and shows better performance than the higher loading of 0.39 mg/cm^2 tested without MPL (**Figure 2a**). The higher interfacial contact area, provided by the MPL, allows the cell to reach its optimal compression at lower compression factor. Indeed, the lowest HFR for the Sintered PTL of 71 mΩ·cm² (**Figure 4c**) occurred at 28% compression factor, whereas for the sintered MPL, the minimum HFR of 67 mΩ·cm² (**Figure 4f**) was reached at 16%. Figure 4**e** shows the evolution of HFR with current density. As summarized in Figure 4**f**, the averaged HFR of the MPL sample decreased from 73 to 67 mΩ·cm² between 0–16% compression factor (**Figure 4f**), while the Sintered PTL showed a higher reduction from 123 to 80 mΩ·cm²(**Figure 4c**), confirming that the improved performance with compression is related to interfacial contact increase between the PTL and the electrode. Here, the HFR values remain above the intrinsic resistivity of the Nafion 212 membrane (50 mΩ·cm²).

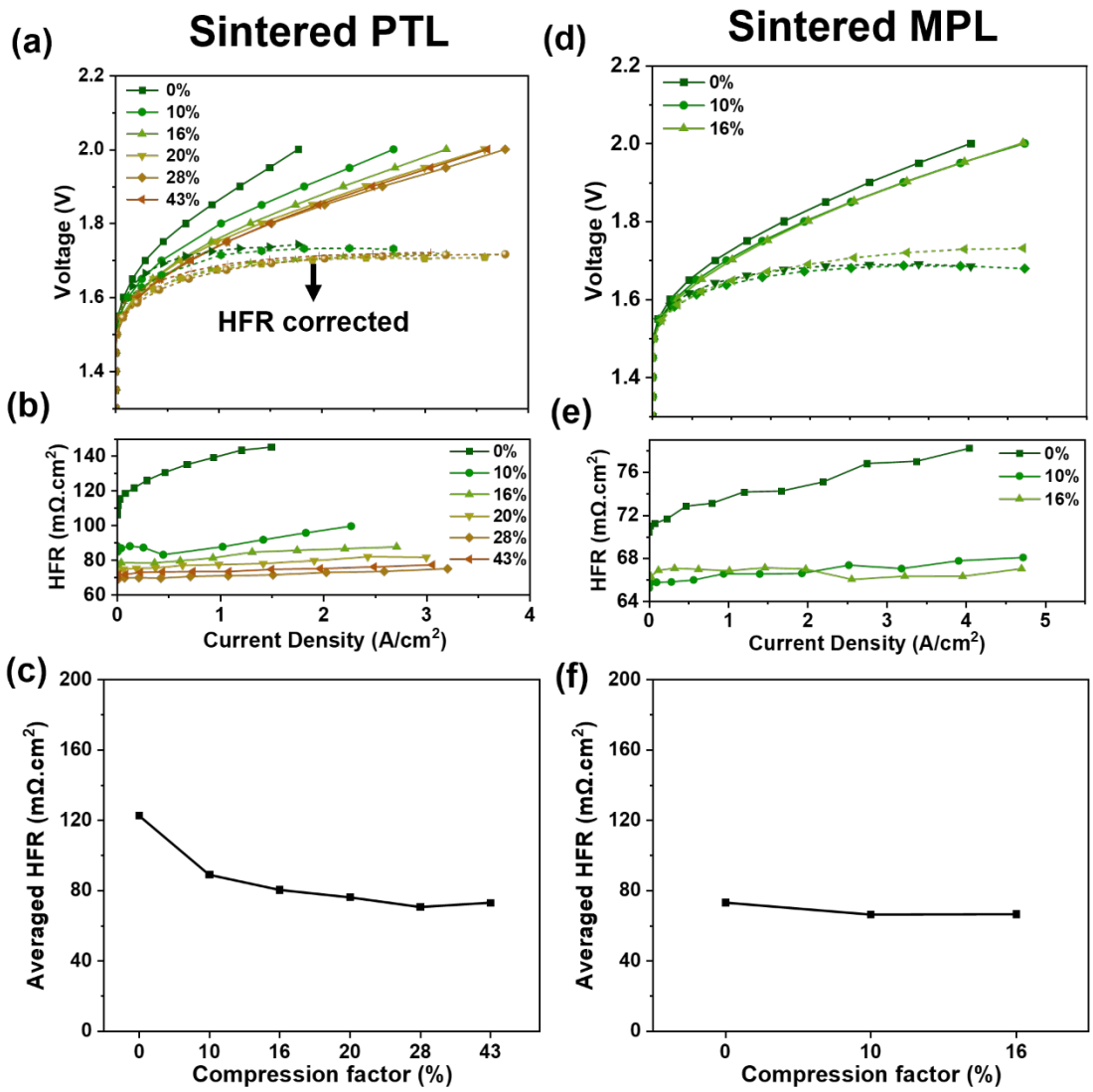

373

374 ***Figure 4***. *Electrochemical characterization data for ultra-low loading (0.14 mg/cm²) Sintered PTL*

375 *with Nafion 212 membrane. a) Polarization curve b) HFR vs current density. c) Averaged HFR as a*

376 *function of compression factor. Sintered MPL with Nafion 212 membrane d) Polarization curve e)*

377 *HFR vs current density. f) Averaged HFR as a function of compression factor.*

378 The evolution of specific surface charge density obtained from CVs for various compression factors

379 is presented in **Figure S3** for the different cell configurations from **Figures 2-4**. Charge density was

380 normalized by the catalyst loading and by the charge measured at 0% compression factor for all

samples to access the deviation of the electrochemical surface area (ECSA) with compression. As shown in **Figure S3**, increasing the compression factor has a minimal effect on the normalized specific charge density for the higher catalyst loading. However, when comparing PTL types at the same loading, the increase in charge density with compression is higher for the Fiber PTL than for the Sintered PTL. The impact of compression is more pronounced for lower catalyst loadings than for higher loadings. ECSA increases by 43% and 8.9% for low and high catalyst loadings, respectively. For the low loading samples, the increase of normalized charge density between Sintered PTL and sintered MPL is similar. These results clearly highlight that the electrode/PTL interface controls the ECSA and the catalyst utilization of the electrode. Adding MPL and improving the compression of the assembly are critical topics to improve performance, especially when decreasing iridium loadings.

Electrochemical cell pressure distribution

We investigated the distribution of pressure within the electrochemical cell for each compression factor using a pressure-sensitive film with a pressure range of 2.5 to 9 MPa. **Figure S7** shows the mapping of the pressure across the active surface area of the electrolyzer cell follows the flow-field pattern. It reveals that the regions under the channels are under-compressed, while the regions under the lands are over-compressed. **Figure S8**, in the SI, shows the normalized surface counts distribution of pressure across the active surface area determined from the pressure maps displayed in **Figure S8a** of the SI. When increasing the compression factor, the area undergoing a pressure below 2.5 MPa is continuously decreasing. It is worth noting that due to the film's low sensitivity, the pressure can lay between 0 to 2.5 MPa. On the other hand, the surface area exposed to higher

pressure, above 8 MPa, increases to reach the film upper limit of 9.5 MPa. Surprisingly, the local pressure within the cell is not increasing gradually but instead, the overall pressure of the cell is increasing because of the higher surface that underwent a pressure of 8 to 9.5 MPa and certainly higher pressure. This evolution is summarized by the **Figure S8b** showing the evolution of the surface fraction exposed to low and high pressure. As the compression factor increases, the ratio of surfaces at high pressure over low pressure increases to reach the surface ratio of land over channel (0.81, highlighted in dashed line on Figure 5b) at 55% compression factor. At this compression factor, all the surface under the land is compressed at a pressure above 8.5 MPa. Throughout the range of compression factors applied to the electrochemical cell, regions were consistently over compressed by over 8 MPa. Therefore, micro-CT will be used to study the effect of such pressure on the electrolyzer assembly's structure.

Micro x-ray Computed Tomography

X-ray micro-CT was employed to study the structural evolution of the membrane and the porous layers upon compression. Tomography images of electrolyzer cells were measured over a set of varied cell compression controlled by the torque applied. For direct comparison with the electrochemical characterization presented previously, a total of 8 cells were investigated. MEAs were assembled with the Fiber PTL and the Sintered PTL using either N115 membrane or N212 membrane. The same MEA configurations were imaged in the 0.65 mm and in the 1 mm width flow-channels in the cell. The pressure of the assembly, calculated from the GDL thickness, is approximated as the local pressure estimated with pressure paper in the electrochemical cell and allows direct comparison.

The images of the Sintered PTL (Figure 5**a**) and the Fiber PTL (Figure 5**b**) with N115 membrane measured in the 0.65 mm cell show that hydration of the membrane leads to significant pressure increase due to the swelling of the membrane that is pushing the GDL into the cathode channel. When increasing the compression in wet anode conditions, the membrane and the GDL became thinner under the land and expanded into the channel. Also, while the Sintered PTL morphology is not changing, mild deformation of the Fiber PTL is witnessed through its bending into the cathode channel. The same observations can be made for the Sintered PTL (Figure 5**c**) or the Fiber PTL (Figure 5**d**) with the N212 membrane. Over all the configurations and across the pressure range, the interface between the membrane and the porous layers is always maintained. Even with the important deformation caused by the compression of the assembly, the interfacial contact area is preserved. Similar trends are witnessed for the sample assembled using the 1 mm width flow channel cell that are presented in **Figure S13** and **Figure S14** of the SI. Therefore, the improvement of the interfacial contact area, suggested by electrochemical characterization, must result from the intrusion of the PTL fibers or particles into the electrode surface that is hardly accessible with micro-CT due to resolution limitation.

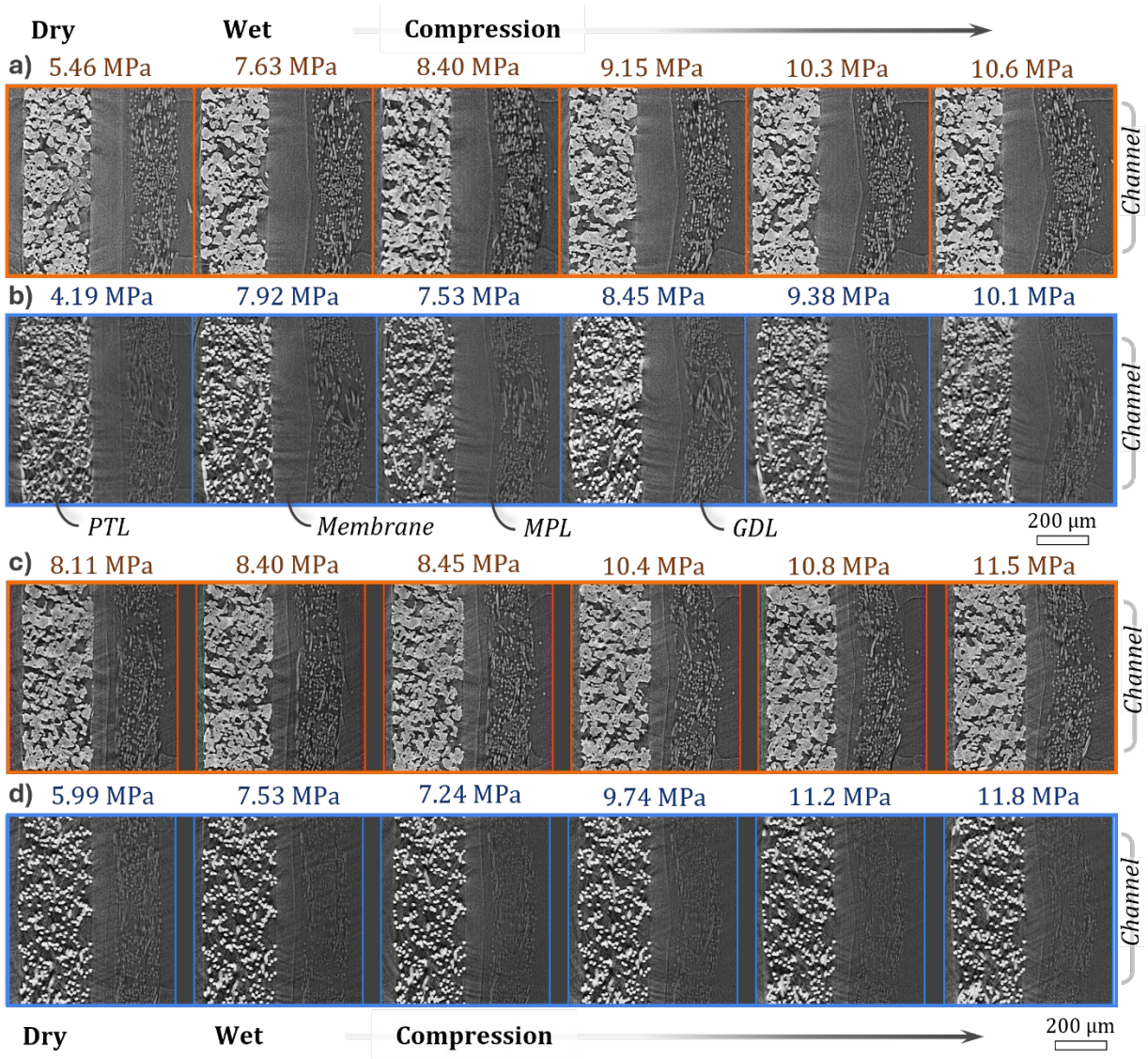

Figure 5. *Cross-sections images of the electrolyzer cell centered on the 0.65 mm wide channel for the assembly made from* ***a)*** *Sintered PTL and Nafion N115,* ***b)*** *Fiber PTL and Nafion N115,* ***c)*** *Sintered PTL and Nafion N112,* ***d)*** *Fiber PTL and Nafion N112.*

The thickness of the membrane was measured across the sample volume, under the land, on both sides of the channel, and in the middle of the channel. For each cell configuration and each pressure, the membrane strain was calculated considering the membrane hydrated thickness of 150 µm and 60 µm for N115 and N212, respectively. The evolution of the membrane strain with pressure is plotted in Figure 6**a** for the 1 mm cell. In the channel, the positive strain shows the membrane expansion, while under the land the membrane is compressing as shown by the negative strain. Increasing pressure leads to higher expansion of the membrane and higher compression under the channel and land, respectively. The same deformation trend of the membrane is observed in the 0.65 mm cell (Figure 6**b**). However, the membrane expansion in the channel is less pronounced in the 0.65 mm cell as the strain is lying between 0.1 and 0.3 at 12 MPa, while it went up to 1.0 for the N212 Sintered sample in the 1 mm cell. Thus as expected, for the same pressure, the membrane will deform more in the cell having a wider channel and compress more under the land.

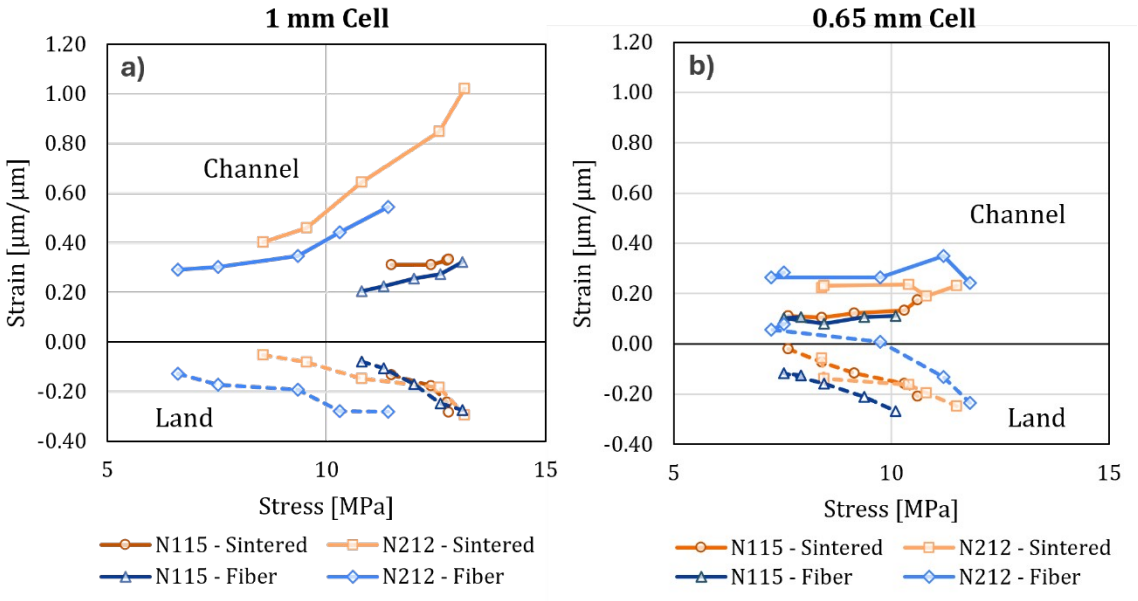

Figure 6. *Strain of the hydrated membrane as a function of stress measured on the 4 cell configurations:* ***a)*** *with the cell having a 1 mm wide channel and* ***b)*** *with the cell having a 0.65 mm wide channel. Strain measured under the land (dashed lines) and under the channel (continuous lines) are plotted.*

The relative position of the PTL and GDL surfaces throughout the volume of the tomographs were determined via image analysis to quantify the deformation of the porous layers with compression. **Figure 7** displays position of the PTL edges and of the surface of the GDL facing the channel for all cell configurations and for the different pressure conditions. Looking at the deformation of the sample with Sintered PTL N115 in 1 mm cell (**Figure 7a**), the Sintered PTL is not affected by the pressure increase. However, the GDL surface deforms significantly, bending into the channel, while the GDL and membrane thickness is decreasing under the land. The same evolution can be observed for all cells having a Sintered PTL (Figure 7**a** to Figure 7**d**). When decreasing the channel width from 1 mm to 0.65 mm, the deformation of the membrane and GDL seems less important. The lower deformation observed in 0.65 mm cells can be explained by the lower pressure applied for equivalent force on 0.65 mm cell due to its higher contact surface area. Indeed, focusing on the Sintered PTL with N212 and comparing its deformation in the 1 mm cell (**Figure 7c**) and in the 0.65 mm cell (**Figure 7d**), it appears that the GDL bending is similar for the same pressure (8.4 MPa and 8.5 MPa). When looking at results with Fiber PTL, a similar behavior is observed with compression (Figure 7**e** to Figure 7**h**). GDL bends in the channel and compresses under the land when increasing the pressure. Even though the deformation is not as important as for membrane and GDL, the Fiber PTL is affected by the compression. Again, the membrane and GDL deformation are more important in the cell having larger channel width due to the increased applied pressure, while using N212

membrane and for similar pressure, similar deformation is observed in the 0.65 mm (**Figure 7g**) and in the 1 mm cell (**Figure 7h**). Therefore, as the deformation of the thin N212 membrane is less affecting the GDL deformation than the N115 membrane, it appears that the GDL deformation due to compression depends mostly on applied pressure and not on channel width.

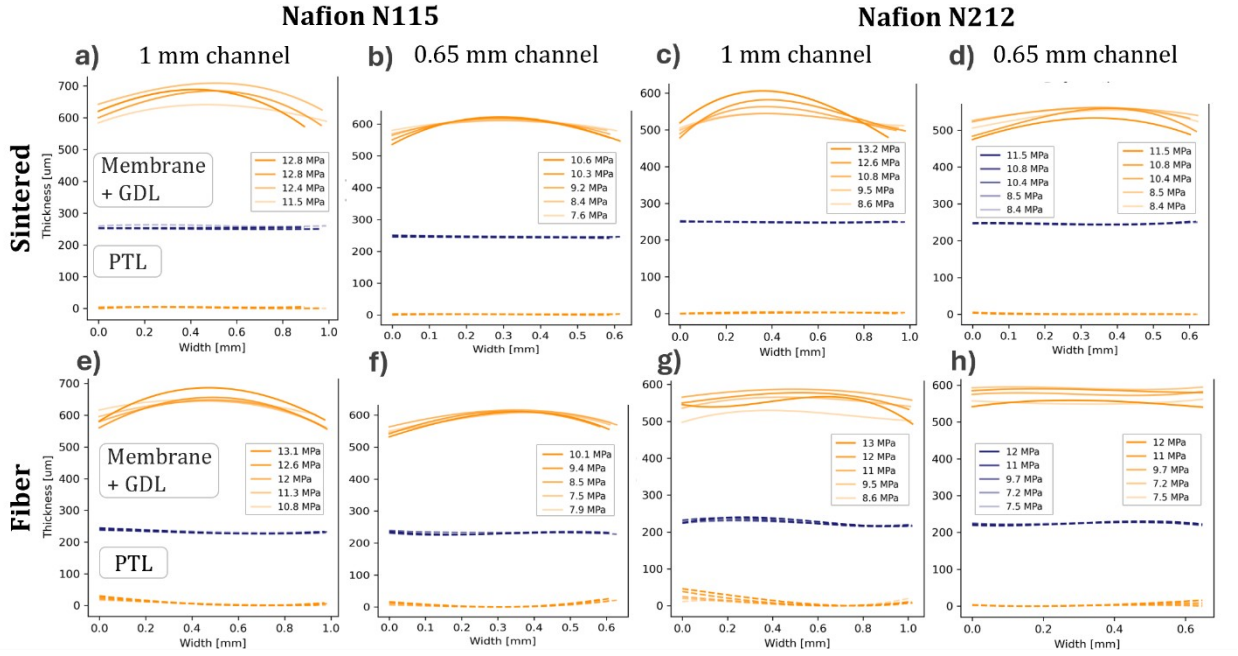

Figure 7. *Deformation of the assembly under the channel measured as the deformation of the edges of PTL and the edge of the GDL facing the channel as a function of compression. Results are presented for the assembly configurations using N115 and N212 with Sintered and Fiber PTL imaged both in the 1 mm cell and the 0.65 mm cell.*

With the deformation of the GDL and membrane varying significantly across the channel width, the average strain of the components across the channel width is studied and compared to the strain at the middle and at the edges of the channel. Specifically, the effect of membrane hydration on the structure of the electrolyzer assembly is depicted by the strain deviation of the GDL and membrane

491 from dry to wet, plotted in **Figure 8a.** The results are presented only for the cell made with the thick
492 N115 membrane where the membrane deformation is contributing more to the measured strain of
493 the GDL and membrane than for the thinner membrane. Within the 1 mm cell, the thickness of the
494 membrane and GDL increase similarly across the channel width with hydration, with no significant
495 deviation between edge and channel locations. The strain increase is directly related to the
496 membrane hydration, initially wet, expanding and increasing the cell assembly pressure. With the
497 0.65 mm cell, the strain increase is more important in the middle of the channel than at the edges.
498 Indeed, as shown previously in the cross-section images (Figure 5) the membrane thickness
499 increases more in the channel than in the land due to the significant constraint that was already
500 applied under the land. The GDL strain caused by hydration is about 2 µm/µm under the land against
501 10 µm/µm in the channel. The same evolution of the strain is seen when using the Fiber PTL (**Figure**
502 **8b**). In the 1 mm cell, the strain increases homogeneously by 9 µm/µm through the channel width.
503 The higher strain observed when using Fiber PTL in comparison to Sintered PTL (2 µm/µm) can
504 result from the initial higher compression of Sintered PTL N115 configuration. Again, with the
505 0.65 mm cell, the expansion of the GDL and membrane is more important within the channel than at
506 its edge. Effect of membrane hydration on the strain of membrane and GDL is not compared
507 quantitively between the 0.65 mm cell and the 1 mm cell as the initial pressure varies and must affect
508 the resulting strain.

509 The evolution of the strain in average and at the two locations (*i.e.* edge, channel) was also studied as
510 a function of pressure. The strain of the GDL and membrane assembled with the Sintered PTL
511 (**Figure 8c)** and with the Fiber PTL (**Figure 8d**) are calculated relatively to the dry uncompress
512 thickness of the GDL and N115 membrane. Since the contact surface area between the cell and the

porous layers is larger for the 0.65 mm cell than for the 1 mm cell, the resulting pressure range is higher within the 1 mm cell. The strain of GDL and membrane assembled with Sintered PTL is presented as a function of the pressure in Figure 8c. Across the channel width of 0.65 mm, the membrane and GDL are compressed over the pressure range applied. However, important strain deviation is observed from the middle of the channel to its edge. While strain remains negative at the edge of the channel, the strain in the middle of the channel becomes null at higher pressure for the 0.65 mm cell and even positive for the 1 mm cell, leading to the expansion of the GDL and membrane as an average across the channel. The same trends are observed with the Fiber PTL (**Figure 8d**). The GDL and membrane are compressed on average for the lower pressure witnessed in the 0.65 mm cell, with the higher pressure measured with the 1 mm cell, the strain increase leads to an average expansion of the GDL and membrane within the channel. Strain is always higher in the middle of the channel than at the edges. Finally, the strain values at the two locations are very similar when using Sintered PTL and Fiber PTL even though their structures are very different, they are not affecting the global deformation of the GDL and membrane significantly.

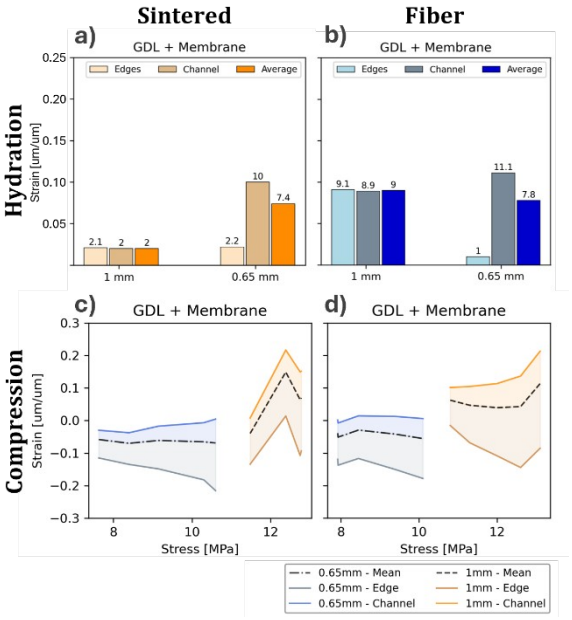

Figure 8. *Effect of hydration on the derformation of the GDL and membrane measured for* ***a)*** *the Sintered PTL and* ***b)*** *the Fiber PTL with the N115 membrane. Deformation of the GDL and membrane as a function of compression for* ***c)*** *the Sintered PTL and* ***d)*** *the Fiber PTL.*

Discussion

Electrochemical characterization of various PEMWE assembly configurations showed that performance increases systematically with compression until an optimal compression factor is reached. Although electrochemical characterization revealed that the improvement in PEMWE performance is primarily due to lower HFR, x-ray micro-CT was used to examine the contact area between the electrodes and the porous layers, as well as membrane deformation.

This study found a similar optimal compression factor lying within 20% and 28 % for several cells, changing the PTL from Sintered to Fiber, decreasing the iridium loading from 0.39 to 0.14 mg/cm^2 and increasing the membrane thickness, using N212 and N115 membranes. While the studies in the literature control the cell assembly pressure by compressing the GDL to 20-30% [11,25,26], our study shows that performance is significantly improved by adding an additional compression factor about 20% to 28% when using bare PTL without MPL, the latter corresponds to about 76 µm decrease in the total gasket thickness for commercial PTLs of 250 µm. At lower compressions the improved performance is most likely due to improved PTL/catalyst layer interface contact. The importance of interfacial contact resistance was observed too by varying PTL types. Polarization improvement was directly correlated to lower HFR and was more significant for MEAs using

sintered PTL instead of more porous fiber PTL and for MEAs with an MPL. As compression increases, the membrane intrudes into the pores of the PTL and the cathode channel, reducing the HFR further. The membrane will flow into the first layer of the PTL pores, as sintered particles and their necks will prevent further flow. No delamination of the cathode/GDL interface was observed through micro-CT with compression. Therefore, the increase in HFR is likely due to the catalyst layer's structural collapse (such as pore-scale collapse) or membrane properties modification (such as lower conductivity with higher compression [30]).

An evaluation of the pressure distribution across the cell surface revealed that the compression achieved through gasket adjustment increases the pressure locally above 8 MPa, while the pressure on the remaining surface area stays below 3 MPa. This estimated local pressure is significantly higher than that reported in the literature [9,14]. However, increasing compression, and thus the surface area exposed to higher pressure, decreases HFR and improves the cell performance. At the optimal compression factor of 28%, 30% of the active surface area is compressed above 8 MPa, while the rest undergoes a pressure below 3 MPa.

Cross-sectional images of the cell assembly acquired from x-ray micro-CT do not show any delamination of the different layers within the pressure range of 4 to 14 MPa. The interfacial contact between the membrane and the porous layers remained intact, despite significant deformation of the GDL, which compresses under the land and expands into the channel. For all cell configurations, compression results in a decrease in HFR and an increase in ECSA. Images of the compressed assembly showed that the Fiber PTL exhibited mild deformation, while the Sintered PTL maintained its shape. Therefore, the performance increase is likely related to the improved contact

571 area, resulting from PTL fibers or particles intrusion into the electrode. This detail is beyond the
572 resolution of micro-CT imaging but has been evidenced by electron microscopy in the literature[27].

573 Performance improvement with compression is more important when using a Fiber PTL, with larger
574 porosity of 63%, and lower contact surface area, and when using lower loadings with lower in-plane
575 connectivity of IrOx particles [28]. Inserting an MPL improves the electrode/PTL contact at low
576 compression, therefore the optimal compression factor of 16% was lower than that of any other cell
577 without an MPL. Optimizing compression and adding an MPL enabled operation of an MEA with a
578 low loading (0.14 mg/cm^2) above 4 A/cm^2 at 2 V, outperforming cells with higher loadings. This
579 highlight how improving interfacial contact determines the electrode ECSA and its performance.

580 A comparison of the cell images from the dry-mounted and hydrated states reveals clear membrane
581 deformation with hydration. This is evidenced by the membrane's expansion within the channel and
582 the higher strain measured under the land. Increasing compression results in higher expansion of the
583 membrane in the channel and it's thinning under the land. Membrane deformation was more
584 significant when using the thicker N115 membrane. Additional compression mildly improved the
585 performance of this cell configuration, showing that hydration and expansion of the thick membrane
586 result in better contact with catalyst layer. At the same time, the average HFR was 118 mΩ·cm² at
587 optimal compression. This value is lower than the membrane's protonic resistivity alone,
588 disregarding electronic resistance. Therefore, membrane deformation initially caused by hydration
589 and enhanced by compression reduces the overall membrane resistivity and ultimately the HFR.

590 Using the expression of the resistance, $R = \rho . \frac{t}{A}$, the equivalent resistance of a deformed membrane
591 can be simulated by Equation 2, considering two resistances in parallel that have different areas (

592 A) and thicknesses (t) but a constant resistivity (ρ). The suffixes refer to the land (l) and to the
593 channel (c).

594 $$\frac{1}{R_{eq.}} = \frac{1}{R_l} + \frac{1}{R_c} = \frac{A_l}{\rho \times t_l} + \frac{A_c}{\rho \times t_c} \quad (2)$$

595 Considering that the total membrane volume $V = A.t$ is constant upon compression, Equation 2 can
596 be rewritten to express the membrane's resistance as a function of the membrane's thickness
597 deviation in the channel while defining the land area (A_l) and the channel area (A_c).

598 $$R^s_{eq.} = \rho \left(\frac{A_c}{t_c} + \frac{A_l^2}{A.t - A_c t_c} \right)^{-1} \times A \quad (2)$$

599 While in our electrochemical cell the channel and land widths are 0.85 and 1 mm respectively,
600 several channel/land widths were used to plot the surface resistance of a membrane as a function of
601 its expansion within the channel as presented in **Figure 9**. The results clearly show that the
602 membrane deformation significantly decreases its resistance within the range of deformation
603 measured from x-ray micro-CT images. Therefore, the important deformation of the N115 upon
604 hydration must explain the low HFR in comparison to the resistance of the uncompressed membrane
605 used for this calculation [24]. Even though the HFR of all assemblies with N212 membranes was
606 above the membrane proton resistance, as already discussed, the deformation of the N212
607 membranes due to compression also contribute to the decrease in HFR, in addition to improved
608 interfacial contact.

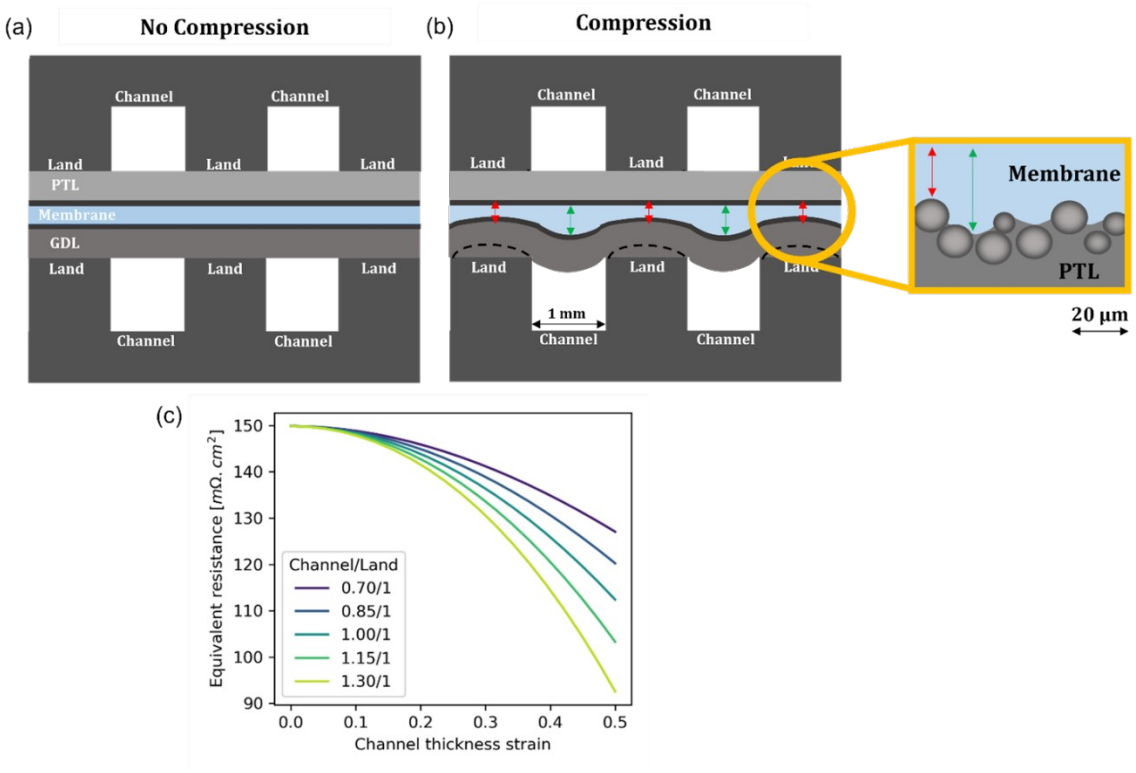

Figure 9. *Schematic for deformation of cell components* ***a)*** *uncompressed and* ***b)*** *with compression.* ***c)*** *Surface resistance of a membrane as a function of the membrane strain under the channel calculated for a land width of 1 mm and channel widths spanning from 0.7 to 1.3 mm.*

Conclusion:

An extensive investigation of the effect of compression on the structure and performance of an electrolyzer was conducted by combining x-ray micro computed tomography and electrochemical characterization of several electrolyzer cell configurations. Specifically, this study investigated the importance of the interface between the PTL and the catalyst layer. Performance was drastically improved by increasing cell compression by about 20 to 30% of the GDL thickness in comparison to the typical compression applied in the literature. Optimizing the cell compression and adding a microporous layer to the titanium PTL enabled the achievement of a high current density of 4.7

A/cm² at 2 V for an electrode with low iridium content (0.14 mg/cm²). Significant deformation was observed using micro-CT imaging. With hydration of the dry assembly, expansion of the membrane in the channel was especially pronounced for the thicker membrane. Higher compression increased membrane deformation and resulted in decreasing the HFR. Cell compression also deforms the GDL under the land and expands it within the channel. However, no delamination of the porous layers or electrodes was observed. Therefore, the improved performance with compression, directly correlated to the HFR decrease, must result from both increased contact at PTL/catalyst layer interface, membrane intrusion into the PTL and membrane deformation into the cathode channel. Since the GDL is the main deforming material, changing its material or thickness may significantly impact the optimal compression of the cell assembly. Although the results of this study can be applied directly, further studies on the effects of compression on membrane and catalyst durability are needed.

Acknowledgments:

The authors acknowledge funding from DOE Energy Earthshot Initiative as part of the Center for Ionomer-Based Water Electrolysis, award DE-AC02-05CH11231. This research used resources of the Advanced Light Source, which is a DOE Office of Science User Facility under contract no. DE-AC02-05CH11231. Florian M. Chabot was supported in part by an ALS Doctoral Fellowship in Residence. Toyota Research Institute North America is acknowledged for funding.

References

Ghavam S, Vahdati M, Wilson IAG, Styring P. Sustainable Ammonia Production Processes. Front Energy Res 2021; 9.

Moradpoor I, Syri S, Santasalo-Aarnio A. Green hydrogen production for oil refining – Finnish case. Renewable and Sustainable Energy Reviews 2023; 175: 113159.

Pivovar B, Rustagi N, Satyapal S. Hydrogen at Scale (H_2@Scale): Key to a Clean, Economic, and Sustainable Energy System. Electrochem Soc Interface 2018; 27: 47–52.

Wang CR, Stansberry JM, Mukundan R *et al.* Proton Exchange Membrane (PEM) Water Electrolysis: Cell-Level Considerations for Gigawatt-Scale Deployment. Chem Rev 2025; 125: 1257–1302.

van Renssen S. The hydrogen solution? Nat Clim Chang 2020; 10: 799–801.

Bernt M, Gasteiger HA. Influence of Ionomer Content in IrO_2/TiO_2 Electrodes on PEM Water Electrolyzer Performance. J Electrochem Soc 2016; 163: F3179–F3189.

Scheepers F, Stähler M, Stähler A *et al.* Improving the Efficiency of PEM Electrolyzers through Membrane-Specific Pressure Optimization. Energies (Basel) 2020; 13: 612.

Mandal M, Moore M, Secanell M. Measurement of the Protonic and Electronic Conductivities of PEM Water Electrolyzer Electrodes. ACS Appl Mater Interfaces 2020; 12: 49549–49562.

Selamet OF, Ergoktas MS. Effects of bolt torque and contact resistance on the performance of the polymer electrolyte membrane electrolyzers. J Power Sources 2015; 281: 103–113.

García-Salaberri PA, Chang H-M, Lang JT *et al.* The critical role of the anode porous transport layer/catalyst layer interface of polymer electrolyte membrane water electrolyzers: A parametric analysis. Chemical Engineering Journal 2025; 509: 160722.

Hasa B, Aryal UR, Higashi S *et al.* Porous transport layer influence on overpotentials in PEM water electrolysis at low anode catalyst loadings. Applied Catalysis B: Environment and Energy 2025; 361: 124616.

Moreno Soriano R, Rojas N, Nieto E, de Guadalupe González-Huerta R, Sandoval-Pineda JM. Influence of the gasket materials on the clamping pressure distribution in a PEM water electrolyzer: Bolt torques and operation mode in pre-conditioning. Int J Hydrogen Energy 2021; 46: 25944–25953.

Frensch SH, Olesen AC, Araya SS, Kær SK. Model-supported characterization of a PEM water electrolysis cell for the effect of compression. Electrochim Acta 2018; 263: 228–236.

Hintzen A, Stähler M, Friedrich I. Membrane Creep Caused by Porous Transport Layer Compression in PEM Water Electrolysis and the Impact on Hydrogen Permeation. J Electrochem Soc 2025; 172: 044512.

Cruz Ortiz E, van Treel N, Koch S, Vierrath S, Bühler M. The effect of compression on PEM Electrolyzer membrane electrode Assemblies. J Power Sources 2024; 614: 235018.

Holzapfel P, Bühler M, Van Pham C *et al.* Directly coated membrane electrode assemblies for proton exchange membrane water electrolysis. Electrochem commun 2020; 110: 106640.

Bazarah A, Majlan EH, Husaini T *et al*. Factors influencing the performance and durability of polymer electrolyte membrane water electrolyzer: A review. Int J Hydrogen Energy 2022; 47: 35976–35989.

Grigoriev SA, Millet P, Korobtsev SV *et al*. Hydrogen safety aspects related to high-pressure polymer electrolyte membrane water electrolysis. Int J Hydrogen Energy 2009; 34: 5986–5991.

Siracusano S, Di Blasi A, Baglio V *et al*. Optimization of components and assembling in a PEM electrolyzer stack. Int J Hydrogen Energy 2011; 36: 3333–3339.

Arthurs C, Kusoglu A. Mechanical Characterization of Electrolyzer Membranes and Components Under Compression. J Electrochem Soc 2024; 171: 094510.

Olesen AC, Kær SK. The Effect of PFSA Membrane Compression on the Predicted Performance of a High Pressure PEM Electrolysis Cell. ECS Trans 2015; 68: 99–116.

Omrani R, Shabani B. Hydrogen crossover in proton exchange membrane electrolysers: The effect of current density, pressure, temperature, and compression. Electrochim Acta 2021; 377: 138085.

MA L, SUI S, ZHAI Y. Investigations on high performance proton exchange membrane water electrolyzer. Int J Hydrogen Energy 2009; 34: 678–684.

Tsampas MN, Pikos A, Brosda S, Katsaounis A, Vayenas CG. The effect of membrane thickness on the conductivity of Nafion. Electrochim Acta 2006; 51: 2743–2755.

Slade S, Campbell SA, Ralph TR, Walsh FC. Ionic Conductivity of an Extruded Nafion 1100 EW Series of Membranes. J Electrochem Soc 2002; 149: A1556.

Liu C, Shviro M, Gago AS *et al.* Exploring the Interface of Skin-Layered Titanium Fibers for Electrochemical Water Splitting. Adv Energy Mater 2021; 11.

Padgett E, Bender G, Haug A *et al.* Catalyst Layer Resistance and Utilization in PEM Electrolysis. J Electrochem Soc 2023; 170: 084512.

Ernst MF, Meier V, Kornherr M, Gasteiger HA. Preparation and Performance Evaluation of Microporous Transport Layers for Proton Exchange Membrane (PEM) Water Electrolyzer Anodes. Electrochem Soc 2024; 171: 074511.

Weber CC, Wrubel JA, Gubler L, Bender G, De Angelis S, Büchi FN. How the Porous Transport Layer Interface Affects Catalyst Utilization and Performance in Polymer Electrolyte Water Electrolysis. ACS Appl Mater Interfaces 2023; 15: 34750–34763.

Kusoglu, A., Hexamer, A. Jiang R., Gittleman, C.S., Weber A.Z., Effect of Compression on PFSA-ionomer Morphology and Predicted Conductivity Changes, Journal of Membrane Science, 2012, 421-422; 283-291